Int. J. Electrochem. Sci., 14 **(2019)** 8662 – 8675, doi: 10.20964/2019.09.31

International Journal of
ELECTROCHEMICAL
SCIENCE
www.electrochemsci.org

In-situ Grown Hierarchical MoS_2 Nanoflakes on Three-Dimensional Carbon Fiber Papers as Free-Standing Anodes for Lithium-Ion Battery

Hongjie Li[1,2], Yi He[1,2,], Qiangbing Yang[3], Jizhuang Wang[1,2], Siming Yan[1,2] and Jingyu Chen[4,*]*

[1] State Key Lab of Oil and Gas Reservoir Geology and Exploitation (Southwest Petroleum University), Chengdu, 610500, China.
[2] College of Chemistry and Chemical Engineering, Southwest Petroleum University, Chengdu, 610500, China
[3] Chongqing Key Laboratory of Environmental Materials & Remediation Technologies, Chongqing University of Arts and Sciences, Chongqing 402160, China.
[4] Deakin University, Institute for Frontier Materials, VIC 3220, Australia.
[*]E-mail: chemheyi@swpu.edu.cn; jingyu.chen@deakin.edu.au

Received: 17 April 2019 / *Accepted:* 28 June 2019 / *Published:* 31 July 2019

Owing to the high capacity of MoS_2, it's considered to be a next-generation lithium ion batteries (LIB) anode material. However, the weak electron transfer limits its application. Herein, hierarchical MoS_2@CFP composite materials based on in-situ grown hierarchical MoS_2 nanoflakes on three-dimensional carbon fiber paper (CFP) is prepared. The hierarchical MoS_2/CFP composites serve as self-supporting electrodes and show potential for improved battery performance. The 1st discharge capacity reached 1332 mAh/g and still reached 703 mAh/g after 100 cycles at a current density of 0.1 A/g. The superior performance of the MoS_2@CFP composites was mainly attributed to the combination of a high capacity ability of MoS_2 and the high electron transport capability of carbon fibers. In addition, this synthetic strategy provides a certain idea for the synthesis of other layered composite materials.

Keywords: MoS_2 nanoflakes, carbon fiber papers, lithium-ion battery, in-situ growth

1. INTRODUCTION

LIBs are considered to be the power source for vehicles for the next generation in recent decades [1, 2]. However, the new LIB anode needs to be developed due to the shortcomings of traditional commercial anodes, such as the low capacity of commercial graphite anodes, and the volume change of commercial silicon anodes when used [3-5]. It is hoped to find a safe, environmentally friendly and natural resource-rich anode with high capacity. Recently, transition metal dichalcogenides (TMDCs) has

received extensive attention owing to the special bidimensional structure [6-9]. The interlayer space between hierarchical structures of TMDCs allows small ions to be inserted/extracted, such as lithium ion, sodium ion and potassium ion [10-12]. Therefore, the TMDCS are considered as ideal anode materials [2].

MoS_2, typical TMDCs' representative and has been extensive researched and applicated in electrocatalysis, photocatalysis, and membrane separation [13-18], etc. The theoretical lithium storage of molybdenum disulfide up to 670 mAh/g, higher than commercial graphite anode (373 mAh/g). In addition, the MoS_2 anodes have little effect on the volume change when it is used. It is because the interlayer spacing of layered MoS_2 is 6.15 Å and can be expanded to 15 Å because of insertion of the remaining Li^+. However, some MoS_2' shortcomings such as weak electron conduction capability, low rate capability and poor cycling stability, limiting its practical application. In order to overcome these obstacles, researchers have explored many ways to increase the capacity of MoS_2 electrodes by combining with different carbon nanomaterials. For example, Chen fabricated MoS_2/ agraphitic carbon composites anode by solvothermal method [19]. Furthermore, Chen and his co-workers fabricated superior performance MoS_2/graphene nanoflake anode by in-situ solution phase reduced method [20]. Similarly, Mai's group reported in-suit growth MoS_2 on reduced graphene oxide (rGO) composites and obtained MoS2/rGO hybrids anode with excellent performance [21]. Lu and co-workers employed inserting Li^+ into bulk MoS_2 and obtained exfoliation of Li_XMoS_2, then coated with dopamine (DOPA) on the single-layer MoS_2 surface and calcinated $(DOPA)_XMoS_2$ under nitrogen to obtain MoS_2/N-doped graphene, which shows a superior performance for Li^+ storage [22]. Mahanty's group mixed MoS_2 with multiwalled carbon nanotube (MWCNTs) and performed multiple milling, then got the MoS_2/WMCNTs hybrids anode, providing a new idea for the preparation of MoS_2/carbon composites [23]. Wang's group went a step further, reported a mixture of MoS_2 and single-carbon nanotubes (SCNTs) by dispersed MoS_2 and SCNTs in N-cyclohexyl-2-pyrrolidone (CHP) and used point probe sonication to blended materials to the composites in CHP, then the MoS_2/SCNTs composites was obtained by filtration through a nitrocellulose membrane under vacuum, which displayed an excellent electrochemical performance [24]. Recently, Chen fabricated a 3D layered MoS_2 nanosheets/carbon nanofiber via sample dip process, then obtained MoS_2/ACF hybrids anodes with a superior performance for Li^+ storage and good discharging/charging cycling stability [25].

Herein, we demonstrate hydrothermal method to fabricate grown multilayer MoS2 nanoflakes on the three-dimensional carbon fiber papers and then obtain the hierarchical MoS_2@CFP composite materials. As a composite material framework and a growth template of MoS_2, CFP has excellent electron and lithium ion transport properties and allows electrons to be transported along the path to MoS_2. The hierarchical MoS_2 structure stabilizes the lithium ion insertion/extraction process in the MoS_2 nanosheet, buffers the volume change of the MoS_2 nanosheet due to its interlayer space and improve the cycle performance. In addition, the MoS2 possess high capacitance. The hierarchical MoS_2@CFP act as self-standing and free-binder anodes, displayed high reversible Li^+ storage capacity and excellent cycling stability.

2. EXPERIMENT

2.1 Chemicals

$(NH4)_6Mo_7O_{24}•4H_2O$ and thiourea were purchased from Kelong Chemical Co. Ltd., Chengdu, China. the chemicals were used as received. Carbon fiber papers (CFP, TORAY, TGP-H-060, 20*20cm) was Saibo New Material Co., Ltd, Hefei, China. The water used in the experiment was deionized water.

2.2 Synthesis of MoS_2@CFP

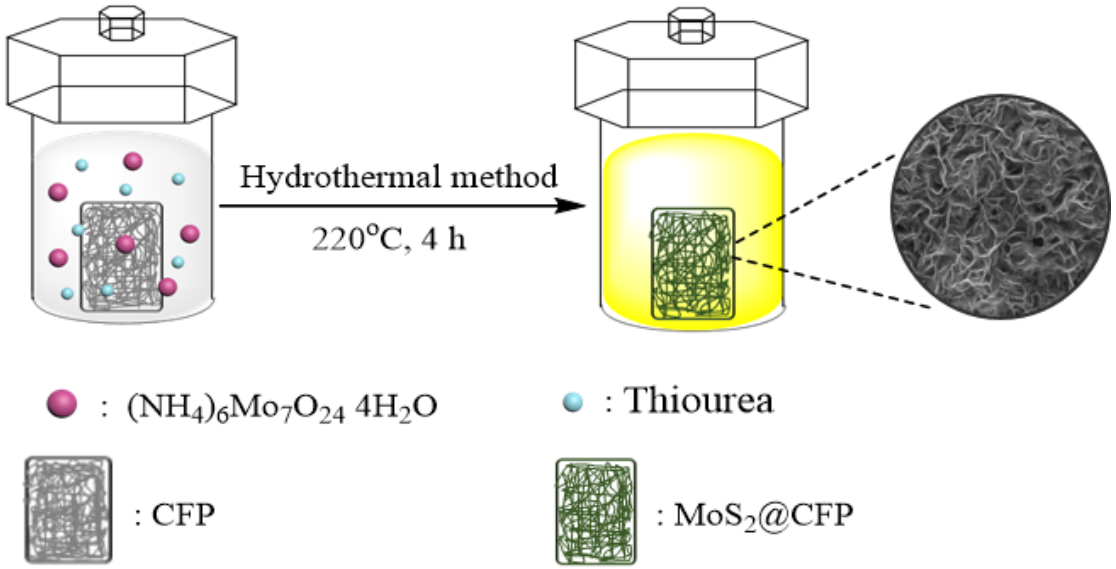

Figure 1. illustration of fabrication of as-designed electrode.

MoS_2 was grown in situ on CFP directly via hydrothermal method [26]. In brief, 0.1235 g $(NH4)_6Mo_7O_{24}•4H_2O$ and 0.1064 g thiourea were dissolved in 70 mL deionized water and then aqueous solution was sonicated for 20 min. After that, Aqueous solution and pre-treated CFP were poured in 100 mL autoclave, then treated at 200℃ for 4 h. The autoclave was naturally cooled to room temperature. Then, the CFP wrapped with MoS_2 was taken out of the autoclave, cleaned with ethanol and then desiccated in vacuum oven at 40°C for 6 hours. Finally, MoS_2@CFP was annealed to obtained more complete lattice MoS_2 at 800℃ with Ar/H_2 atmosphere for 2h.

2.3 Characterization

Composition test of the as-prepared MoS_2@CFP was using X-ray diffraction (XRD, PANalytical), with Cu Ka radiation at 40KV. Raman analysis was measured by Raman spectrometer (LabRAM HR800), with a laser excitation wavelength at 266 nm. Chemical state of the sample was characterized by an X-ray photoelectron spectrometer (XPS, AXIS SUPRA), with Al Ka. The sample's morphology was obtained by the Scanning Electron Microscope (SEM, HITACHI) and Energy dispersive Spectroscopy (EDS) mapping scans. And the surface morphology was further characterized through transmission-electron microscopy (TEM, HITACHI).

2.4 Electrochemistry test

The electrochemical ability of as-designed electrode performed via coin cells test (CR-2032). A piece of MoS_2@CFP as work electrode, with lithium metal as both the counter and reference electrode and Celgard 2400 membrane as the separator, the electrolyte containing 1 mol/L $LiPF_6$ in a mixture of ethylene carbonate (EC), diethyl carbonate (DEC) and Ethyl methyl carbonate (EMC) ($V_{EC}/V_{DEC}/V_{EMC}$ = 1:1;1). The tested cells were assembled in an argon filled glovebox. The galvanostatic charged and discharged test of the cell recorded between 0.001 V and 3.0 V on a LAND CT2001A battery tester (Wuhan LAND electronics Co., Ltd, China). The other electrochemical tests are using CHI660D electrochemical workstation (CH Instruments, China). Impedance tests are using Electrochemical impedance spectroscopy (EIS).

3. RESULTS AND DISCUSSION

Fig. 1 synoptically declares the preparation of the in-suit grown hierarchical MoS_2 nanoflakes on the surface of CFP. It can be obtained that the petal-like structure, which shows the in suit anisotropic growth of the ultrathin hierarchical MoS_2 on the CFP surface.

Fig. 2a exhibits the XRD pattern of the samples. CFP has very strong peaks which is truncated for amplification of other peaks. CFP has very strong peaks which are truncated for amplification of other peaks. The peaks appearing in 26.2° and 54.8° can be indexed to highly carbonized carbon fiber [14]. The diffraction pattern of the in-situ grown MoS_2 has peaks at 14.2° and 34.6° are attributed to (002) and (101) planes of hexagonal MoS_2 [24]. The (002) diffraction is related to a d-spacing of 0.62 nm which is consistent with the TEM images.

The Raman analysis of MoS_2@CFP as displayed in Fig. 2b. The peaks at 378 and 402 cm^{-1}, corresponding to E^1_{2g} and A_{1g} modes of the hexagonal MoS_2, respectively [25]. The Raman shifts are from the first order Raman vibration modes with the S-Mo-S layer. Previous studies have shown that Raman chromatography can estimate layer number of hierarchical MoS_2 by two adjacent Raman shift peaks, and the gap value of MoS_2@CFP is 25 cm^{-1}, showing that MoS2 maintains an ultra-thin state with only a few layers [27-29].

The XPS profiles of Mo and S as shown in Fig. 2c and 2d. Fig. 2c shows a high-resolution spectrum of Mo. The peaks at 229.0 and 232.0 eV can be attributed to the dual states of Mo^{4+} $3d_{3/2}$ and Mo^{4+} $3d_{5/2}$, the peaks have a separation energy close to 3.1 eV, which is characteristic of the Mo species. There is a weak peak about 236.0 eV, corresponding to Mo^{6+}, indicating that there is little Mo' oxidation. The peak at 226.0 eV corresponds to the S 2s component of MoS_2. The Peaks of 161.7 eV and 163.0 eV were observed in S 2p spectrum displayed in Fig. 2d, attributing to S^{2-} $2p_{3/2}$ and S^{2-} $2p_{1/2}$, respectively. In addition, the peak around 2.3 eV compared to the $2p_{3/2}$ (164.1 eV) and $2p_{1/2}$ (165.2 eV) peaks of element S, which is a typical 2p shift of S in MoS_2. [30, 31].

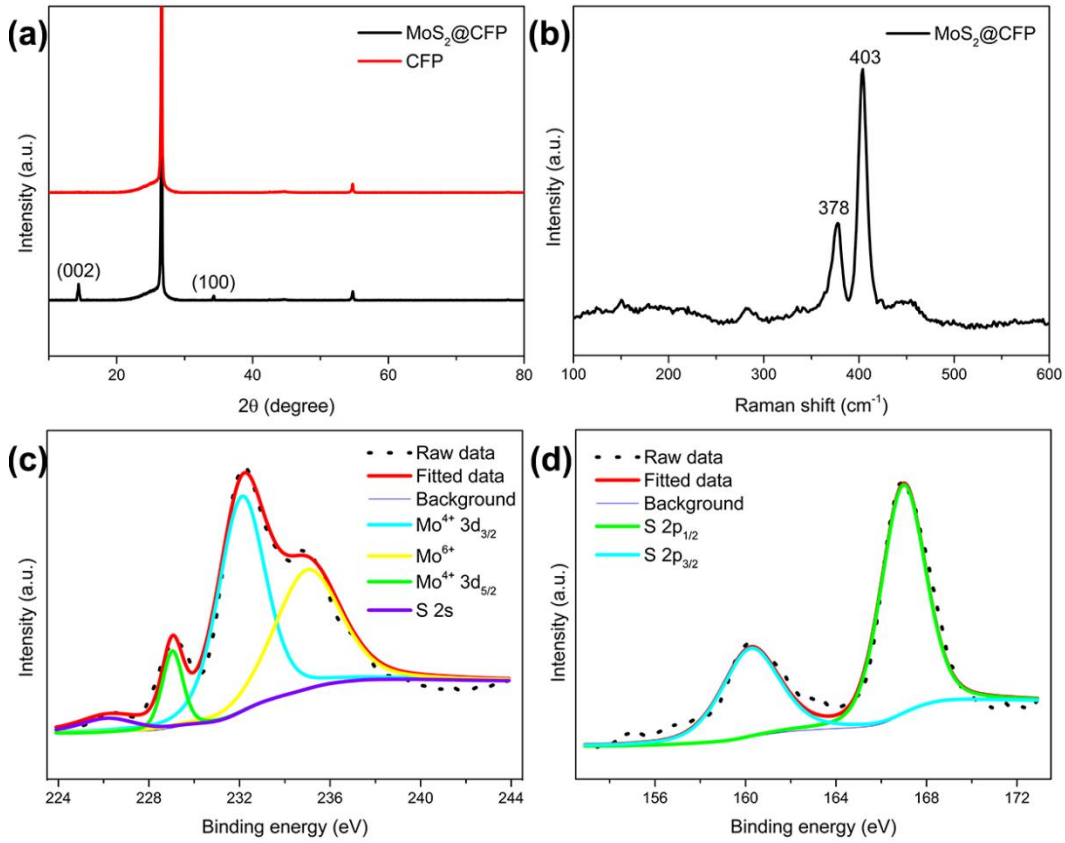

Figure 2. (a) XRD patterns of the samples; (b) Raman spectra of the samples; The XPS spectra of the samples, (c) the Mo 3d XPS spectrum and (d) S 2p XPS spectrum.

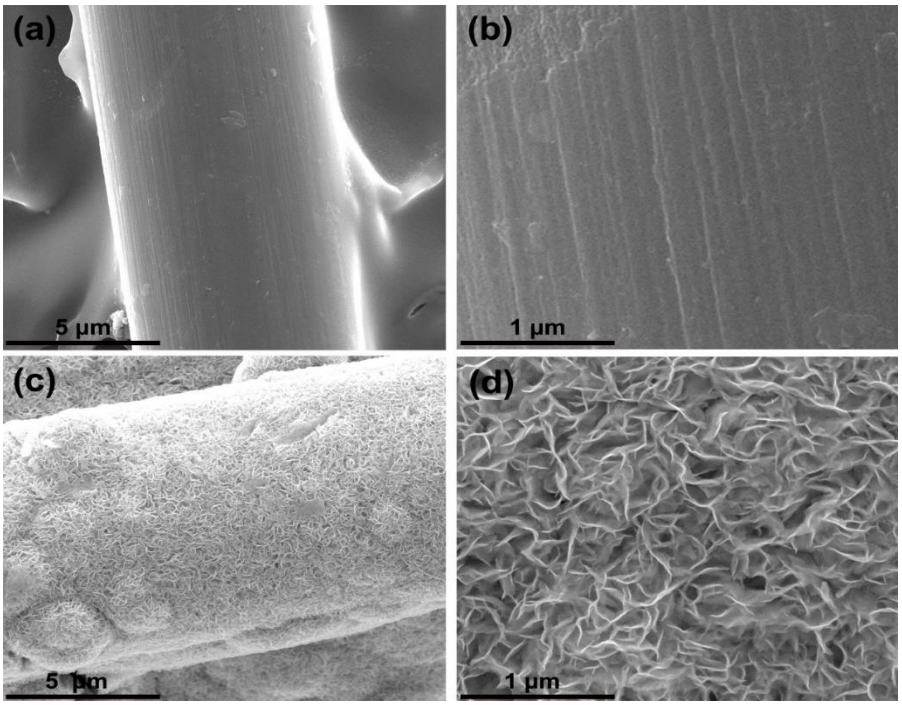

Figure 3. (a-b) SEM images of the original CFP; Figure 3(c-d) SEM images of the as-prepared MoS_2@CFP.

The morphology of the CFP and hierarchical MoS_2@CFP were obtained by investigated by SEM and TEM analyses. From the low-magnification Fig. 3a we can observe a single carbon nanofiber and the diameter of the single fiber is about 7nm. High-magnification SEM images (Fig. 3b) shows the nanofiber's smooth surface morphology. After CFP was surface-modified by MoS_2, the surface of the material becomes rougher as exhibited in Figure 3c. In addition, Fig. 3d shows the petal-like MoS_2 nanoflakes occupied the surface of the CFP. The hierarchical structure on the surface of the electrode facilitate the insertion and extraction of Li^+.

EDS mapping images (Fig. 4) shows the distribution of elements for hierarchical MoS_2@CFP. The element distribution is evenly on the electrode surface (Fig. 4a), large number of homogeneous MoS2 nanoflakes cover the surface of the carbon fiber. In such a nanomaterial structure, the good transmission performance of carbon fiber to electrons compensates for the poor conductivity of MoS_2, which is benefit for lithium battery performance.

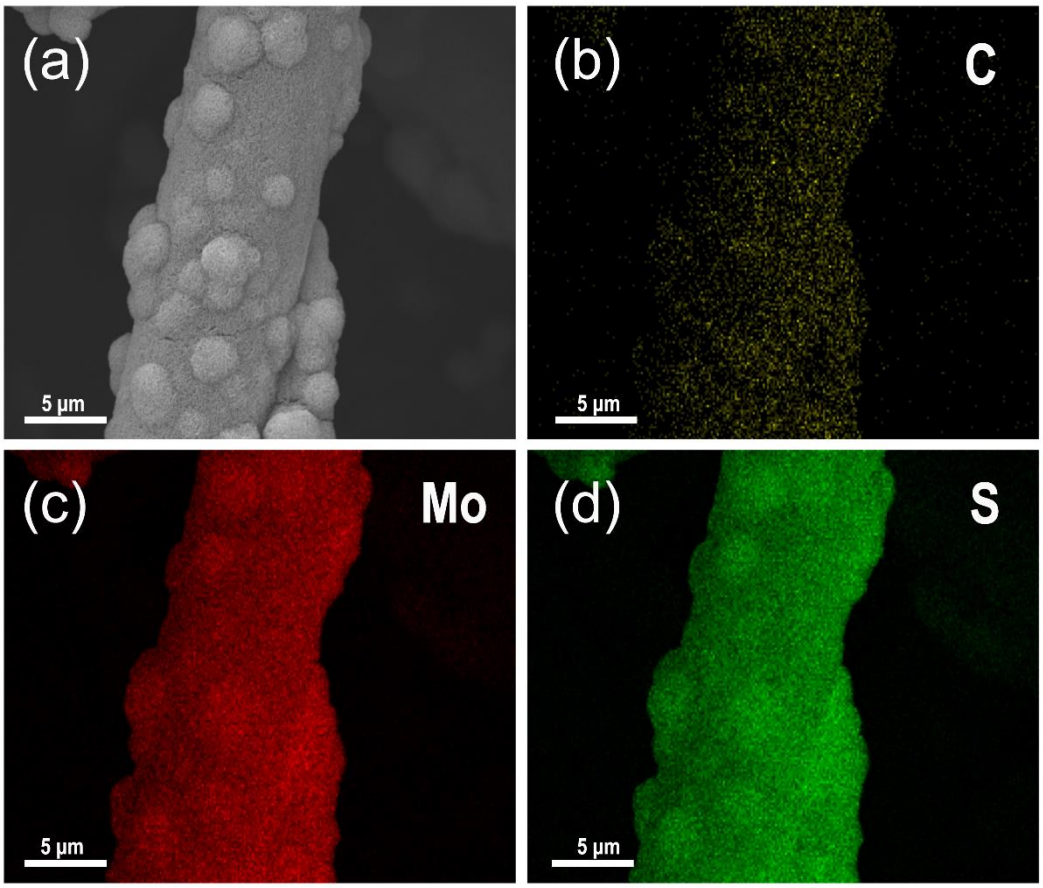

Figure 4. (a) SEM image and the EDX mapping displays elements distribution of C (b), Mo (c) and S (d) of MoS2@CFP.

TEM observed surface morphology of the molybdenum disulfide. The hierarchical nanostructure of MoS_2@CFP presented in the SEM images are difficult to observe clearly in the TEM images because the sample is dispersed in EtOH by ultrasound in TEM sample-fabrication process. TEM images shows the flower-like hierarchical MoS_2 nanoparticle (Fig. 5a) and the petal -like MoS_2 nanoflakes grew in

different directions, which all should be perpendicular to the surface of the CFP (Fig. 5b). In Fig. 5c, MoS_2 nanoflake' thicknesses are only several nanometers. Moreover, the high resolution TEM image (Fig. 5d) further points out the clear interlayer structure of hierarchical MoS_2 that an interlayer spacing of 0.62 nm can be indexed to (002) planes and another interlayer distance of 0.27 nm can be attributed to (100) planes, which are consistent with the XRD analysis of the MoS_2 crystal.

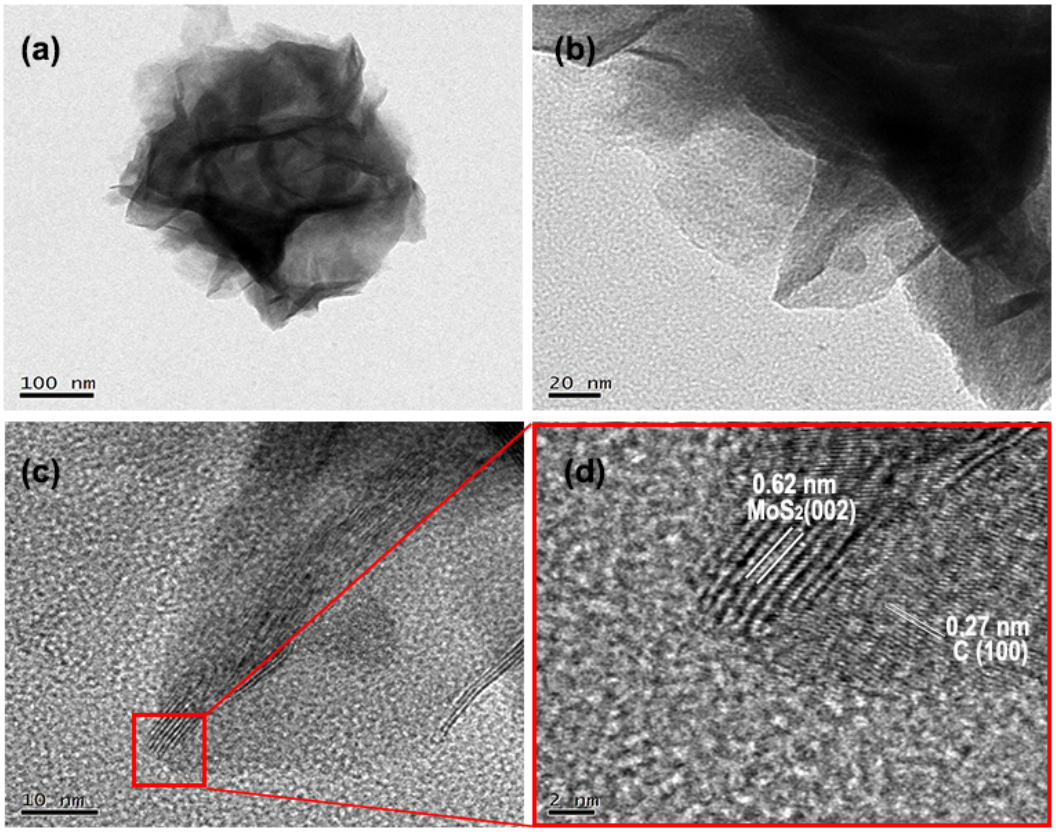

Figure 5. nanostructure of the MoS_2@CFP. TEM images (a) and (b); HRTEM images (c) and (d).

The hierarchical MoS_2@CFP composite has a unique architecture combining one-dimensional carbon nanofibers with two-dimensional MoS_2 nanoflakes, which is potential for excellent lithium battery performance. Fig. 6a displays the first three times cyclic voltammograms curves of the electrode obtained at a scan rate of 0.2 mV/s between a voltage range of 0.001 V and 3.0 V vs. Li^+/Li. Displayed the CVs of the 1st lap is diverse from other circles. For the first cycle curve, a board peak located at 0.95 V is correspond to phase transition from triggered phase to octahedral phase. Generally, a peak at around 0.95 V is related to the insertion of Li^+ into layers of MoS_2, forming Li_XMoS_2 and transforming MoS_2 from 2H to 1T [25, 32]. Another cathodic peak from the first cycle curve about 0.45 V due to Li_XMoS_2 is reducted to form Li_2S and Mo [32-34]. In addition, it is related to form solid electrolyte interface (SEI) due to the electrode material reacts with the electrolyte. At anodic sweeps, the oxidation-peak located at 1.75V, corresponding to Mo is oxidized to MoS_2. And the peak at around 2.42 V is attributed with the

Li_2S oxidation to S. Hence the electrode material would be divided into MoS_2, Mo, Li_2S and S after the cycles[20, 34-37].

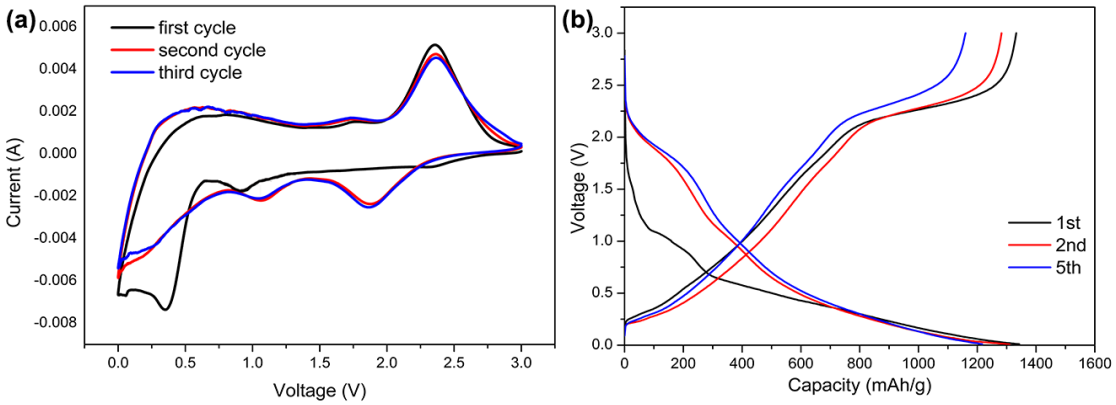

Figure 6. (a) CV curves of the MoS_2@CFP electrode; (b) The galvanostatic charge-discharge (GCD) curves of the MoS_2@CFP electrode.

For subsequent cathodic scan, the shape of the redox potential is completely different from that observed at the1st cycle. The minimum at 0.45 V evaporated, and correspondingly new peak at around1.10 and 1.85 V appeared, which indicates a multistep Li^+-insertion mechanism. In addition, the peak about 1.85 V is associated with the conversion of elemental sulfur to polysulfide and then to Li_2S. The peak at around 1.10 V is related to the reaction of Li with Mo. According to recent reports, Li will form a coordination bond around Mo. The second and third cycles of CV curve are basically overlapping, proving a good reversibility of the MoS_2@CFP electrode [24, 34, 38].

Fig. 6b exhibits the GCD curves for the 1st, 2nd and 5th curve at a current density of 0.1 A/g between 0.001 V and 3.0 V. It can be obtained two clear terraces about 1.19 and 0.69 V during the initial discharge course, usually considered to be two lithiations and confirmed the insertion of ions. The Li^+ embed into the MoS_2 nanosheets and formed Li_xMoS_2. Another two plateaus located at 2.2-2.4 V suggests the reversible Li^+ extraction during the charge process. Furthermore, the peaks located near 2.29 V is also considered to be the Li_2S' oxidation [39, 40].

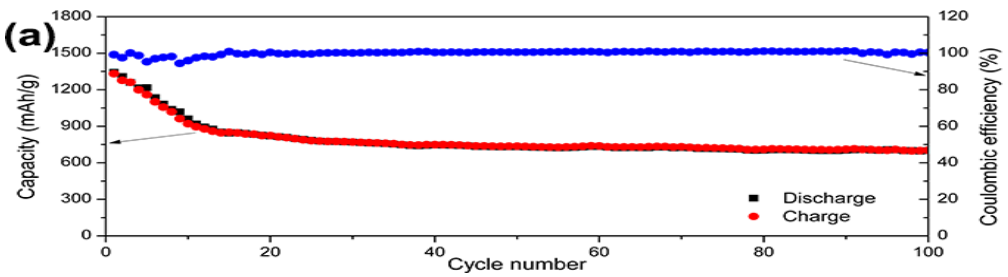

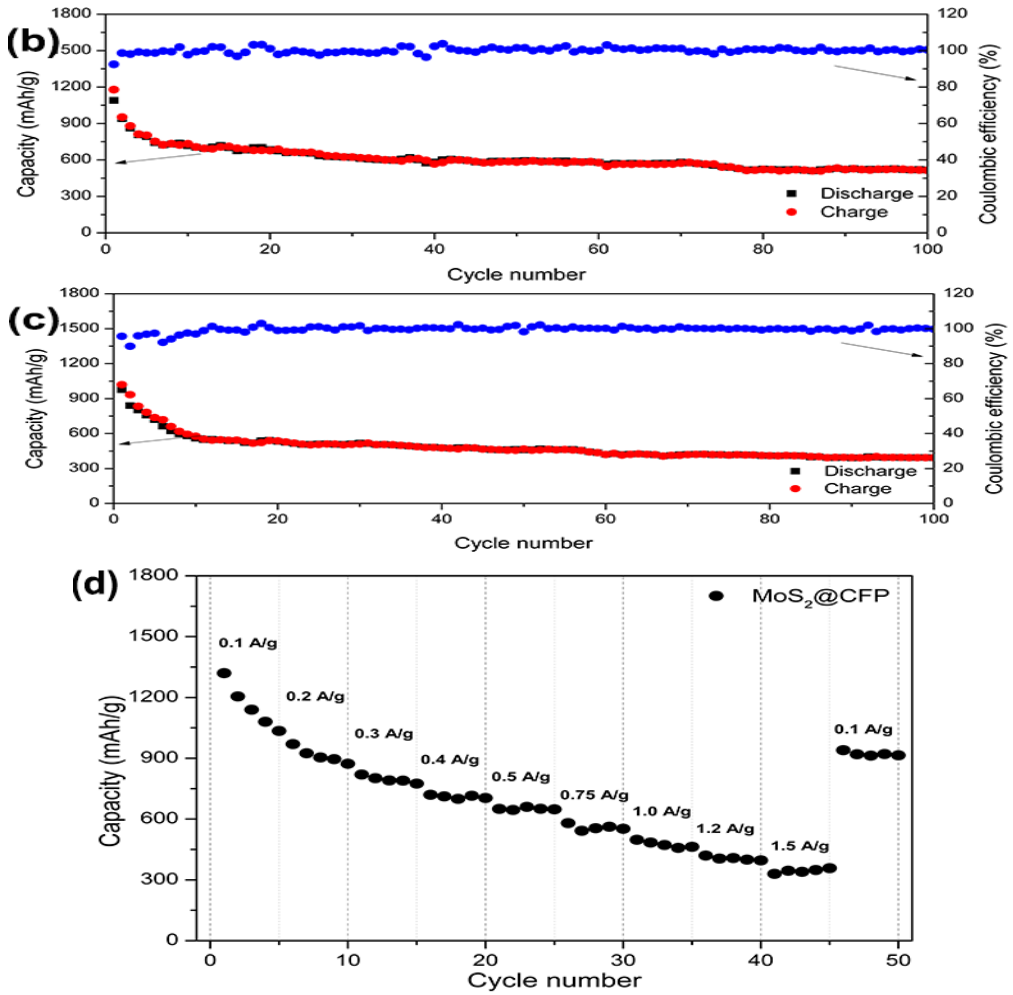

Figure 7. Cycling performance of the MoS_2@CFP at different current density: 0.1 A/g (a), 0.2 A/g (b) and 0.5 A/g (c); (d) Rate performance of the MoS_2@CFP 0.1 to 1.5 A/g.

As-prepared hierarchical electrode performs a good potential for application to electrode materials. Generally, the cycle performance and rate performance are used to indicate the lithium storage capacity. Fig. 7a, 7b and 7c separately show the charge (ion-extraction) and discharge (ion-insertion) curve of the MoS_2@CFP electrode for 100 cycles at the current density of 0.1 A/g, 0.2 A/g and 0.5 A/g. In the first cycle, the capacities are 1332, 1091and 976 mAh/g at 0.1, 0.2 and 0.5 A/g. And after 100 cycles, the MoS_2@CFP electrode separately exhibits reversible discharge capacity of 703, 517 and 392 mAh/g at 0.1, 0.2 and 0.5 A/g. The hierarchical MoS_2@CFP composite shows an excellent cycling performance which compared with the normal CFP and MoS_2 electrodes. The comparison results of the as-prepared hierarchical MoS_2@CFP composite electrodes and the previously reported MoS_2 composite electrodes are shown in table S1. It can be observed that the performance of the prepared electrode is superior even compare with the previously reported MoS_2 composite electrodes.

Fig. 7d exhibits the rate performance at different current density from 0.1 to 1.5 A/g for the MoS_2@CFP electrode. The specific capacities are 1325, 976, 823, 734, 652, 595, 498, 431 and 337 mAh/g at different current density. And after cycles at different current density, the hierarchical MoS_2@CFP composite maintains capacity of 358 mAh/g. Furthermore, as-prepared MoS_2@CFP

electrode also shows good capacity recovery after rate test. When the cycles returned to 0.1 A/g, the capacity is restored to 915 mAh/g after several cycling at current variation from 0.1 to 1.5 A/g.

EIS is used to explore the reason of prepared hierarchical MoS_2@CFP electrodes have such excellent performance and Li^+ storage and insertion dynamics. The Nyquist plots of electrodes before and after 100 cycles at a current density of 0.1 A/g are displayed in Fig. 8a. It can be obtained that the charge transfer resistance reduced after 100 cycles. The Nyquist plots are also fitted by the equivalent circuit model as displayed in Fig. 8b. The fitting parameters of the impedance are listed in Table 1. For the MoS2/CFP electrode before cycles and after cycles, the Rs value is dropped from 23.3 Ω to 22.5 Ω; the Rct value is dropped from 547.9 Ω to 323.0 Ω; and the Rf value is 153.6 Ω after cycles. It is confirmed that the combination of MoS_2 and carbon fiber significantly enhances the electrical conductivity of MoS_2 and thus accelerates the transport of electrons during the insertion/extraction of lithium ions.

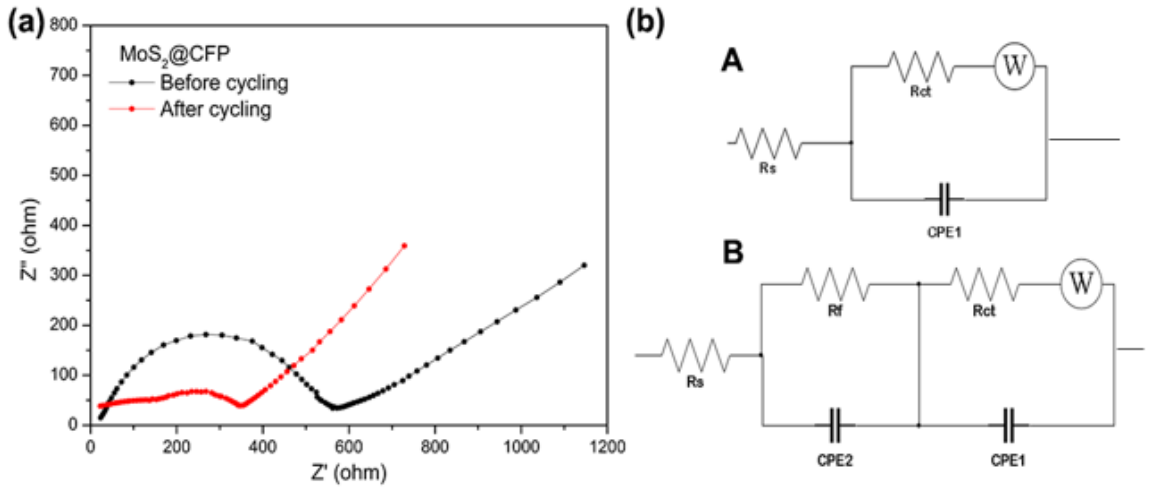

Figure 8. (a) Nyquist plots of the electrode; (b) Equivalent circuit model corresponding to the Nyquist plots of electrode: (A) before, (B) after cycling.

Table 1. Impedance fitting parameters recorded by the equivalent circuit model for the MoS2/CFP electrode before cycles and after cycles.

Electrode	Rs(Ω)	Rct(Ω)	CPE1(μF)	Rf(Ω)	CPE2(μF)
MoS_2@CFP before cycling	23.3	547.9	32.3		
MoS_2@CFP after cycling	22.5	323.0	2.43	153.6	24.7

4. CONCLUSION

In summary, the hierarchical MoS_2@CFP electrodes are fabricated by typical solvothermal method and then calcination in Ar/H_2 atmosphere at 800°C. The hierarchical MoS_2 in suit grew in nanoflakes on three-dimensional carbon fiber papers. Experimental results showed that the hierarchical MoS_2@CFP electrodes have high specific capacitance and excellent stability. The discharge capacity at 0.1 A/g achieved 1332 mAh/g in the 1st cycle and only attenuated to 703 mAh/g after 100 cycles. The three-dimensional CFP provides an electronic transmission path to MoS_2, and the hierarchical MoS_2 has

good Li-ions storage capacity. The synergistic effect of MoS_2 and CFP leads to excellent electrochemical performance of the hierarchical MoS_2@CFP electrode. The type of material should have good application potential in areas such as catalysis, supercapacitors, and membrane science.

SUPPORTING MATERIAL

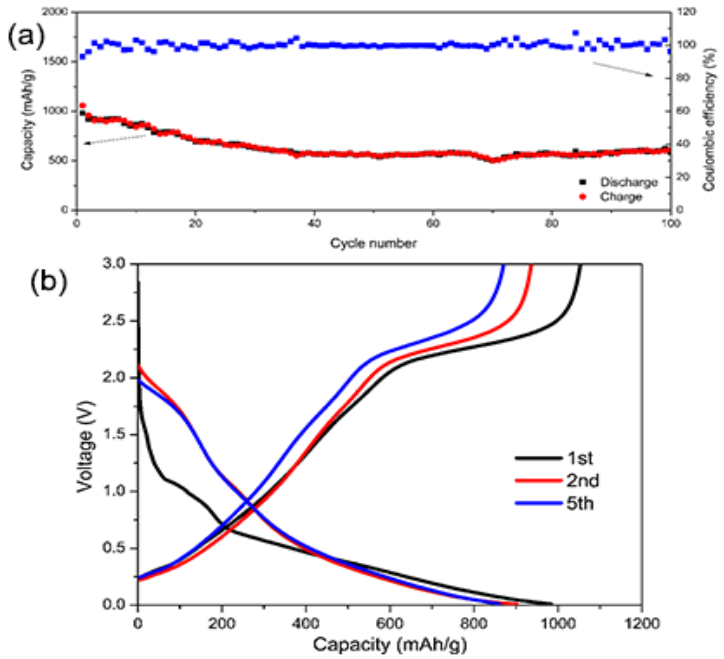

Figure 1s. (a) Cycling performance of the MoS_2 electrode at a current density of 0.1 A/g; (b) The GCD curve of the MoS_2 electrode.

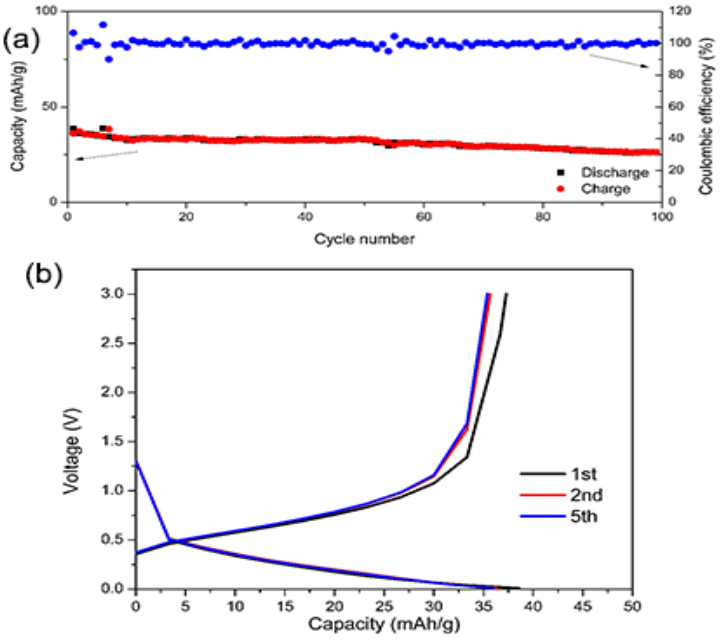

Figure 2s. (a) Cycling performance of the CFP electrode at a current density of 0.1 A/g; (b) The GCD curves of the CFP electrode.

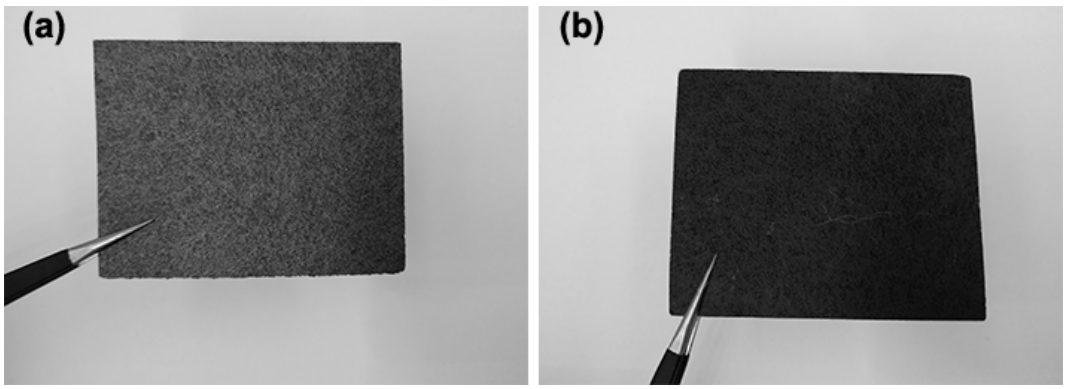

Figure 3s. Photographic images of the CFP (a) and the hierarchical MoS2@CFP (b).

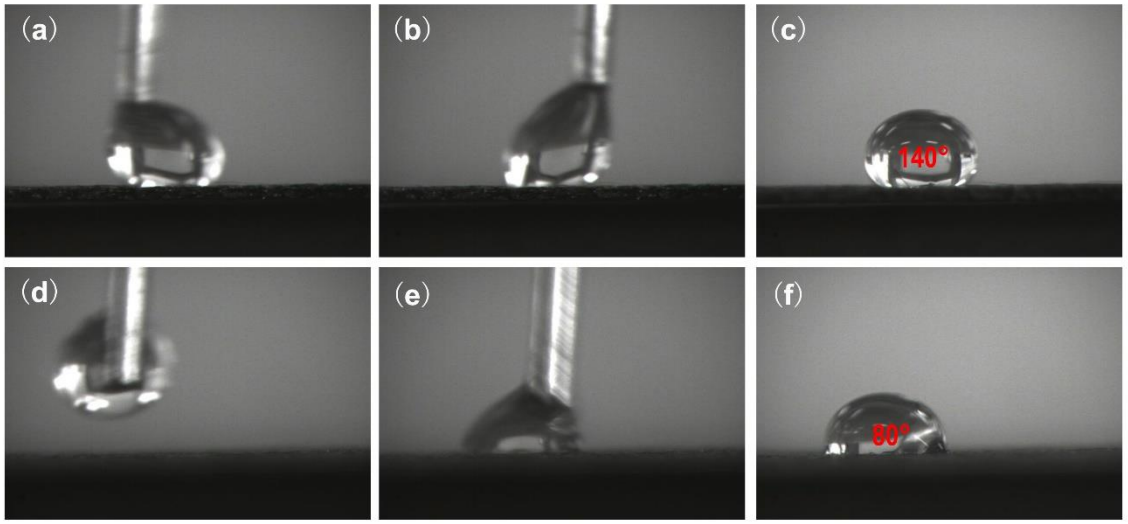

Figure 4s. Water contact angle of the CFP (a, b and c) and t the hierarchical MoS_2@CFP (d, e and f).

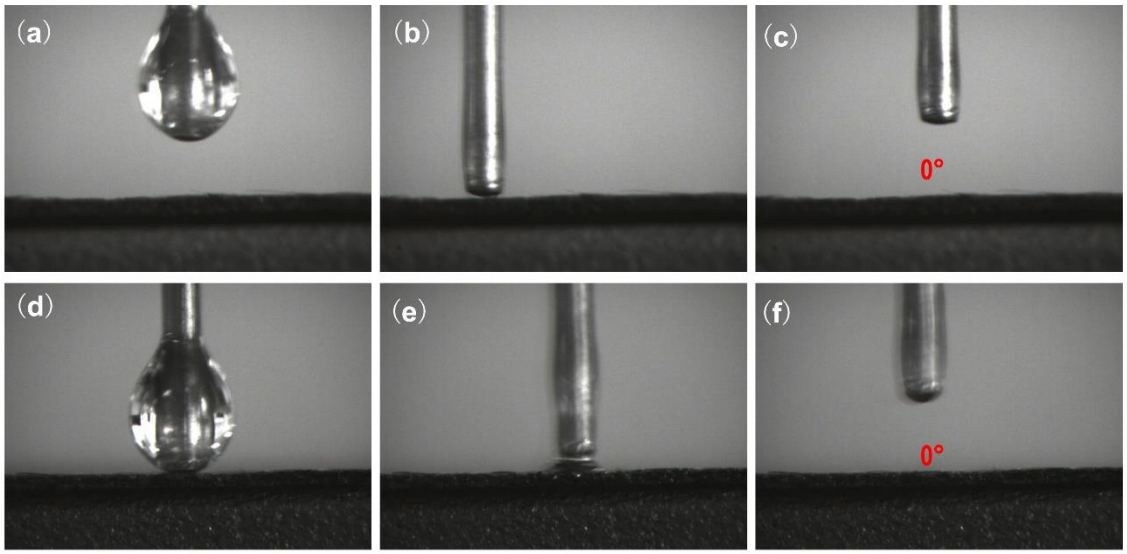

Figure 5s. Oil contact angle of the CFP (a, b and c) and the hierarchical MoS_2@CFP (d, e and f).

Table S1. Performance comparison of the as-prepared hierarchical MoS_2@CFP composite electrodes and the previously reported MoS_2 composite electrodes.

Anode material	DCG performance of 1st cycle (current density: 0.1 A/g): mAh/g	DCG performance after 100 cycles (current density: 0.1 A/g): mAh/g	References
This work	1332	703	
MoS2/amorphous carbon	961	912	19
MoS2/graphene	1300	1290	20
MoS2/rGO	1225	680	21
MoS_2/N-doped graphene	1050	630	22
MoS2/WMCNTs	1214	1030	23
MoS2/SCNTs	825	446	24
MoS2/ACF	1392	971	25

ACKNOWLEDGEMENTS

This work was financially supported by National Natural Science Foundation of China (No.51774245), Applied Basic Research Program of Science and Technology Department of Sichuan Province (No.2018JY0517), Sichuan Province sci-tech Supported project (2015RZ0023) and Youth science and technology creative group fund of Southwest Petroleum University (2015CXTD03).

References

1. J. Xu, H.R. Thomas, R.W. Francis, K.R. Lum, J. Wang and B. Liang, *J Power Sources*., 177 (2008) 512.
2. L. Ji, Z. Lin, M. Alcoutlabi and X. Zhang, *Energ Environ Sci*., 4 (2011) 2682.
3. M.K. Song, S. Park, F.M. Alamgir, J. Cho and M. Liu, *Mat Sci Eng R*., 72 (2011) 203.
4. L. Lu, X. Han, J. Li, J. Hua and M. Ouyang, *J Power Sources*., 226 (2013) 272.
5. M.A. Hannan, M.S.H. Lipu, A. Hussain and A. Mohamed, *Renew Sust Energ Rev*., 78 (2017) 834.
6. M. Fontana, T. Deppe, A.K. Boyd, M. Rinzan, A.Y. Liu, M. Paranjape and P. Barbara, *Sci Rep-UK*., 3 (2013) 1634.
7. W. Bao, X. Cai, D. Kim, K. Sridhara and M.S. Fuhrer, *Appl Phys Lett*., 102 (2012) 042104.
8. M. Chhowalla, H.S. Shin, G. Eda, L.J. Li, K.P. Loh and H. Zhang, *Nat Chem*., 5 (2013) 263.
9. J.H. Yu, H.R. Lee, S.S. Hong, D. Kong, H.W. Lee, H. Wang, F. Xiong, S. Wang and Y. Cui, *Nano Lett*., 15 (2015) 1031.
10. J. Xiao, D. Choi, L. Cosimbescu, P. Koech, J. Liu and J.P. Lemmon, *Chem Mater*., 22 (2010) 4522.
11. H. Zhe, W. Lixiu, Z. Kai, W. Jianbin, C. Fangyi and T. Zhanliang, *Angew Chem Int Edit*., 53 (2015) 12794.
12. X. Ren, Q. Zhao, W.D. Mcculloch and Y. Wu, *Nano Res*., 10 (2017) 1313.
13. Q. Yang, Y. He, Y. Fan, F. Li and X. Chen, *J Mater Sci-Mater El*., 28 (2017) 7413.
14. Q. Yang, Y. He, Y. Fan, X. Chen and Y. Li, *Int J Hydrogen Energ*., 42 (2017) 6482.
15. J. Wang, Y. He, Q. Yang, H. Li, Z. Xie, Y. Fan and J. Chen. *Int J Hydrogen Energ*., 44 (2019) 13205.
16. Q. Yang, Y. He, C. Zou, J. Wang, H. Li and D. Qing, *J Solid State Electr*., 22 (2018) 2969.
17. A. Achari, S. Sahana and M. Eswaramoorthy, *Energ Environ Sci*., 9 (2016) 1224.
18. C. Chen, Y. He, G. Xiao, Y. Xia, H. Li and Z. He, *Appl Surf Sci*., 444 (2018) 511.

19. K. Chang, W. Chen, L. Ma, H. Li, H. Li, F. Huang, Z. Xu, Q. Zhang and J.Y. Lee, *J Mater Chem*., 21 (2011) 6251.
20. K. Chang and W. Chen, *Chem Commun*., 47 (2011) 4252.
21. F. Xiong, Z. Cai, L. Qu, P. Zhang, Z. Yuan, O.K. Asare, W. Xu, C. Lin and L. Mai, *ACS Appl Mater Inter*., 7 (2015) 12625.
22. C. Zhao, X. Wang, J. Kong, M.A. Jia, P.S. Lee, Z. Liu and X. Lu, *ACS Appl Mater Inter*., 8 (2016) 2372.
23. K. Bindumadhavan, S.K. Srivastava and S. Mahanty, *Chem Commun*., 49 (2013) 1823.
24. Z. Wang, T. Chen, W. Chen, K. Chang, L. Ma, G. Huang, D. Chen and J. Lee, *J Mater Chem A*., 1 (2013) 2202.
25. C. Wang, W. Wan, Y. Huang, J. Chen, H.H. Zhou and X.X. Zhang, *Nanoscale*, 6 (2014) 5351.
26. C. Feng, J. Ma, H. Li, R. Zeng, Z. Guo and H. Liu, *Mater Res Bull*., 44 (2009) 1811.
27. H.S. Lee, S.W. Min, Y.G. Chang, K.P. Min, T. Nam, H. Kim, J.H. Kim, S. Ryu and S. Im, *Nano Lett*., 12 (2012) 3695.
28. K.K. Liu, W. Zhang, Y.H. Lee, Y.C. Lin, M.T. Chang, C.Y. Su, C.S. Chang, H. Li, Y. Shi and H. Zhang, *Nano Lett*., 12 (2012) 1538.
29. Y.H. Lee, X.Q. Zhang, W. Zhang, M.T. Chang, C.T. Lin, K.D. Chang, Y.C. Yu, J.T. Wang, C.S. Chang and L.J. Li, *Adv Mater*., 24 (2012) 2320.
30. S.K. Park, S.H. Yu, S. Woo, B. Quan, D.C. Lee, M.K. Kim, Y.E. Sung and Y. Piao, *Dalton T*., 42 (2013) 2399.
31. J. Kibsgaard, Z. Chen, B.N. Reinecke and T.F. Jaramillo, *Nat Mater*., 11 (2012) 963.
32. M. Wu, J. Zhan, K. Wu, Z. Li, L. Wang, B. Geng, L. Wang and D. Pan, *J Mater Chem A*., 5 (2017) 14061.
33. H. Liu, D. Su, R. Zhou, B. Sun, G. Wang and S.Z. Qiao, *Adv Energy Mater*., 2 (2012) 970.
34. X. Jie, X. Wang, X.Q. Yang, S. Xun, L. Gao, P.K. Koech, J. Liu and J.P. Lemmon, *Adv Funct Mater*., 21 (2011) 2840.
35. S.K. Park, S.H. Yu, S. Woo, J. Ha, J. Shin, Y.E. Sung and Y. Piao, *Crystengcomm*, 14 (2012) 8323.
36. K. Chang and W. Chen, *J Mater Chem*., 21 (2011) 17175.
37. G. Du, Z. Guo, S. Wang, R. Zeng, Z. Chen and H. Liu, *Chem Commun*., 46 (2010) 1106.
38. H. Hwang, H. Kim and J. Cho, *Nano Lett*., 11 (2013) 4826.
39. S. Liang, J. Zhou, J. Liu, A. Pan, Y. Tang, T. Chen and G. Fang, *Crystengcomm*, 15 (2013) 4998.
40. Y.M. Chen, X.Y. Yu, Z. Li, U. Paik and X.W. Lou, *Sci Adv*., 2 (2016) 1600021.